



Communication

Electron hybridization and anharmonic thermal vibration effect on structure transition of SrTiO₃ at high-pressure and low-temperature

Takamitsu Yamanaka^{a,b,*}, Muhtar Ahart^c, Ho-kwang Mao^{a,c}, Takeyuki Suzuki^d^a Center for High Pressure Science and Technology Advanced Research, Shanghai 201203, China^b Department of Earth and Space Science, Graduate School of Osaka-University, 1-1 Machikaneyama, Toyonaka, Osaka 560-0043, Japan^c Carnegie Institution of Washington Geophysical Laboratory, 5251 Broad Branch Rd N.W., Washington, DC 20015, USA^d Comprehensive Analysis Center, Institute of Science and Industrial Research, Osaka University, 8-1 Mihogadake, Ibaraki, Osaka 567-0047, Japan

ARTICLE INFO

Keywords:

Structure transition at high-pressure and low-temperature
 Anharmonic thermal vibration
 d - p - π hybridization electron density
 Molecular orbital calculation

ABSTRACT

We execute electron density analysis of SrTiO₃ at low temperatures up to 80 K and high pressures up to 11.88 GPa using X-ray single-crystal diffraction and *ab initio* quantum chemical molecular orbital (MO) calculation. By changing pressures, the cubic SrTiO₃ with perovskite structure goes through a antiferroelastic distortion to tetragonal symmetry above the critical pressure $P_c=7$ GPa with $c/a < 1$ and decreasing with increasing pressure. On the other hand, by changing temperatures, the tetragonal distortion occurs below the critical temperature $T_c=105$ K with $c/a > 1$ and increasing with lowering temperature.

Difference Fourier (D-F) synthesis experimentally proves the residual electron densities $\Delta\rho(xyz)$ are associated with two different effects: electron hybridization bonding electron and anharmonic thermal vibration atoms. The d - p - π hybridization between Ti(3d) and O(2p) orbitals is confirmed in the residual electron density, which is deformed from the ideal spherical density conducted by the atomic scattering factor f_i using Hartree–Fock (HF) approximation. MO calculation also reveals the electron hybridization. Anharmonic thermal vibration of atoms yields a large effect to the structure transition. Mulliken charges analysis of MO calculation indicates much smaller charges than their formal ionic charges. Their ionicity increases from cubic to tetragonal above P_c and below T_c .

1. Introduction

Structure changes of ferroelectric crystals under extreme conditions are often induced from the phonon-electron interaction. An antiferro-distortive phase transition of SrTiO₃ (STO) at 105 K was reported [1–3]. At low-temperatures below around 37 K, soft phonon anomaly and quantum fluctuation for the transition were suggested by electron paramagnetic resonance and dielectric measurement [4–6]. A superconducting state was confirmed [7]. Optical investigations by Raman and infrared spectroscopy have been also executed for STO at low temperature [8,9]. First principles calculation proposed the transition from ferroelectric to antiferro-distortion in tetrahedral phase [10–13]. *Ab initio* molecular orbital calculation (MO) has been intensively undertaken to elucidate the dynamical structure change [14,15]. Evidence for a phase transition of STO on (001) surface at low-temperature was proved by reflection high-energy electron diffraction (RHEED) [16].

A cubic-tetragonal phase boundary is proposed by the Landau theory of phase transitions with the coupling effect between the order

parameter and the volume spontaneous strain [8]. The phase transition mechanism is characterized by the distortion and tilt of the TiO₆ octahedra in the tetragonal phase with nonlinear couplings between the structural order parameter and the volume strain as a function of the applied pressure [17–19].

Experimental determination of the charge density in cubic STO has been reported by studies employing synchrotron [20], laboratory X-rays [21] and γ -ray diffraction at room temperature [22].

The topological analysis of the electron density of STO was discussed based on the X-ray diffraction study at 145 K and theoretical calculation using the density functional formulae [23]. The analysis of the kinetic and potential energy density, derived from the electron density, reveals the stabilizing crystal-forming role of the O atoms in STO. Structural homeomorphism between the experimental electron density and the potential and kinetic energy densities is observed [24]. Calculations of electron densities are carried out from X-ray diffraction data [25].

We aim to elucidate static atomic positional disorder using X-ray single-crystal diffraction experiment of STO at low temperatures and

* Corresponding author at: Center for High Pressure Science and Technology Advanced Research, Shanghai 201203, China.

E-mail address: takamitsu.yamanaka@cap.ocn.ne.jp (T. Yamanaka).

high pressures. Difference Fourier synthesis discloses the residual electron density distribution in consideration of bonding electrons and anharmonic thermal vibration. Quantum chemical MO calculation is also undertaken to confirm the effective charge of atoms at the transition under low-temperature and high-pressure conditions.

2. Experiment

Sample preparation of single crystal STO is described in [Appendices](#). Sample preparation gives large effects on structure transition and Curie point.

Single crystal diffraction study was undertaken using four-circle diffractometer of RIGAK AFC7 with point detector of scintillation counter on 18 kW rotated anode X-ray generator. The highly collimated beam is applied for diffraction experiments under extreme conditions. Precise diffraction intensity measurement at low-temperatures down to 80 K was undertaken using Solvay cycle cryorefrigerator with pressure-swing absorption (PSA) nitrogen gas generator. Diffraction studies at ambient pressure, 1.35 GPa and 5.10 GPa for cubic phase, 7.38, 10.28 and 11.88 GPa for tetragonal were made using diamond anvil cell [DAC] which was especially designed for single crystal diffraction study [26]. Pressure is measured by the ruby fluorescence system [27].

The structure factor F_{obs} is expressed by

$$F_{cal}(\vec{h}) = K \sum_j a_j f_j(\vec{h}) \sum_{js} T_{js}(\vec{h}) \exp\{2\pi i(hx_{js} + ky_{js} + lz_{js})\} \quad (1)$$

Atomic scattering factor f_j of j atom was provided by Hartree–Fock approximation. Anomalous dispersion parameters were taken into account in $f = fo + \Delta f' + i\Delta f''$. The least-squares refinement is conducted by minimization of Δ : $\Delta = \sum_{\vec{h}} w(\vec{h}) \{|F_{obs}(\vec{h})| - |F_{cal}(\vec{h})|\}^2$

3. Result and discussion

We investigate structure transition from paraelectric STO to antiferroelectric phase at low-temperature and high-pressure. The lattice constants were determined by least-square calculation based on the peak refinement of 25 reflections of the single-crystal diffraction. The lattice constant changes as a function of temperature and pressure are presented in [Tables A.1 and A.2](#) in [Appendices](#). The transition pressure (P_c) from cubic to tetragonal phase is at about 7 GPa and in the low-temperature experiments the transition temperature (T_c) is about 100 K. These P_c and T_c are in a good agreement with previously reported data [7].

In order to clarify the pressure and temperature dependence of the lattice constants, two compression curves are presented in [Fig. 1](#) with the tetragonal lattice constants normalized in the cubic setting. The compression of a and c of the tetragonal phase are noticeably decreased at high-pressures in comparison with those at low-temperature. The ratio of c/a of the tetragonal phase in high-pressure with c/a

<1 becomes more extreme with increasing pressure above P_c . On the other hand, the ratio at low temperature below T_c is c/a

>1 and increases with lowering temperature. The observed lattice constants and atomic positions of two phases at high-pressure and low-temperature are listed in [Tables A.1 and A.2](#) in [Appendices](#) respectively. The tetragonal structures are formed by rotation of TiO_6 octahedron around the c axis due to the displacement of oxygen atoms.

Bond distances of Ti–O and Sr–O in the antiferroelectric tetragonal phase ($I4/mcm$ $z=4$) are related to the displacement of oxygen coordinate. The O atomic position in the cubic phase is changed to $\text{O1}(0\ 0\ 1/4)$ and $\text{O2}(x\ x + 1/2\ 0)$ $x=0.25+\Delta$ in the tetragonal phase. Two Ti–O1 distances enormously decrease in the tetragonal structure at both low-temperature and high-pressure. On the other hand, four Ti–O2 increase with pressure. These changes are induced from the rotation of four O2 in the (001) plane with keeping the four-fold

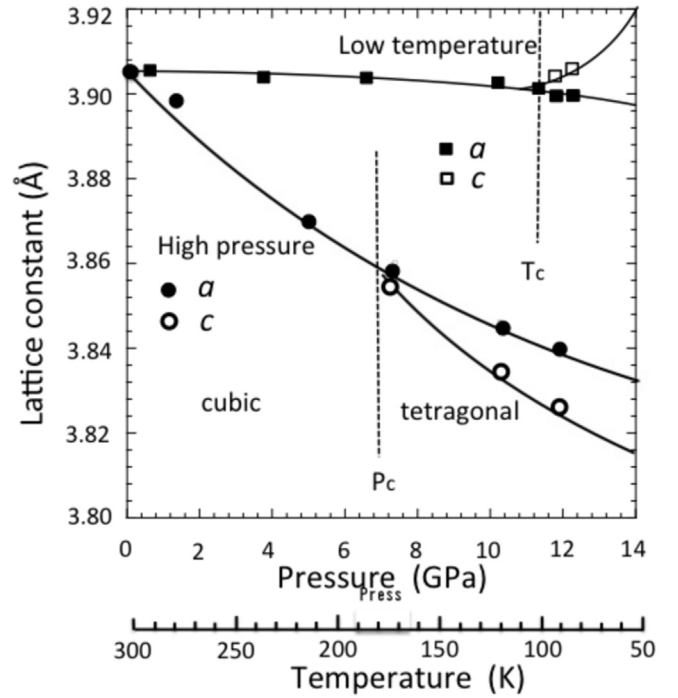


Fig. 1. Solid and open circles respectively indicate the lattice constants of a and c from the high-pressure and low-temperature experiments. The lattice constants of a_t^* and c_t^* of the tetragonal phase are normalized to the pseudocubic lattice ($a_t^*=1/\sqrt{2}a_{tet}$ and $c_t^*=1/2c_{tet}$). The error in the lattice constant is less than the presented circles and squares.

rotation axis. The rotation is more extended with increasing pressure. The bond distance ratio of Ti–O2/Ti–O1 of the tetragonal phase induces the distortion of octahedron of TiO_6 . The ratio increases with elevating pressure. Consequently the distortion is more enhanced with pressure. The bond distance ratio of the tetragonal phase at high-pressure is much larger than at low-temperature, as shown in [Table 1](#). Since the rotation induced by the compression is related to c/a

<1 in the tetragonal phase, the more rotation promotes the distinct changes. The bond distance changes with pressure and temperature are presented in [Fig. A.1](#) in [Appendices](#). Every four Sr–O1 and Sr–O2 distances in the tetragonal phase remarkably decreases with pressure above P_c , although Sr has twelve coordinations with O in the cubic phase.

Pressure effect to the structure is much more remarkable than thermal effect. Average bond $\langle \text{Sr–O} \rangle$ is much more compressed than $\langle \text{Ti–O} \rangle$ under the both conditions. The measurable tolerant factor of $t = \frac{\langle \text{Sr–O} \rangle}{\sqrt{2} \langle \text{Ti–O} \rangle}$ using the average bond lengths in [Table 1](#) decreases with compression and cooling. The factor proves a more deformation of tetragonal lattice with these conditions.

4. Electron density distribution

Difference Fourier synthesis (D-F) of $\{|F_{obs}(hkl)| - |F_{cal}(hkl)|\}$ discloses the deformation electron density (ED) distribution. The residual ED $\Delta\rho(xyz)$ expresses the nonspherical deformation electron cloud by

$$\Delta\rho(xyz) = \frac{1}{V} \sum_h \sum_k \sum_l \{|F_{obs}(hkl)| - |F_{cal}(hkl)|\} \exp\{-2\pi i(hx + ky + lz)\} \quad (2)$$

The atomic scattering factor f_i in the structure factor $F(hkl)$ applies Hartree–Fock approximation, which is composed of the spherical ED distribution model of only one atom in the space without any interaction from the nearest neighbor or second neighbor atoms. D-F maps based on the harmonic oscillator model of atomic vibration show

Table 1

Bond distance. The numbers in parentheses denote errors of the last dismal. Tolerant factors are obtained from the observable average bond distances.

| Bond distance at high-pressure condition | | | | | | | |
|--|----------|----------|----------|----------|----------|----------|----------|
| Press (GPa) | (Sr–O) | Sr–O1×4 | Sr–O2×2 | (Ti–O) | Ti–O1×2 | Ti–O2×4 | Tolerant |
| Cubic <i>Pm3m</i> | | | | | | | |
| 0.0001 | 2.761(2) | | | 1.952(2) | | | 1.000 |
| 1.35 | 2.757(2) | | | 1.949(2) | | | 1.000 |
| 5.10 | 2.736(3) | | | 1.934(3) | | | 1.000 |
| tetragonal <i>I4/mcm</i> | | | | | | | |
| 7.38 | 2.669(3) | 2.612(3) | 2.727(3) | 1.931(3) | 1.922(3) | 1.935(3) | 0.977 |
| 10.28 | 2.572(3) | 2.431(2) | 2.713(3) | 1.945(3) | 1.909(3) | 1.963(3) | 0.935 |
| 11.88 | 2.523(3) | 2.339(2) | 2.706(3) | 1.957(3) | 1.894(2) | 1.988(3) | 0.912 |
| Bond distance at low temperature | | | | | | | |
| Temp (K) | (Sr–O) | Sr–O1×4 | Sr–O2×2 | (Ti–O) | Ti–O1×2 | Ti–O2×4 | Tolerant |
| Cubic <i>Pm3m</i> | | | | | | | |
| 300 | 2.761(5) | | | 1.952(5) | | | 1.000 |
| 190 | 2.761(5) | | | 1.952(5) | | | 1.000 |
| 120 | 2.760(6) | | | 1.951(6) | | | 1.000 |
| 100 | 2.758(6) | | | 1.960(6) | | | 1.000 |
| Tetragonal <i>I4/mcm</i> | | | | | | | |
| 95 | 2.630(6) | 2.759(6) | 2.500(7) | 1.977(6) | 1.952(6) | 1.989(5) | 0.941 |
| 85 | 2.603(6) | 2.755(6) | 2.451(5) | 1.986(6) | 1.988(6) | 2.003(5) | 0.927 |

the deformation of ED around Sr and Ti atomic positions in the projection on to (001). Aspherical residual ED distributions are recognized around the Ti position at ambient conditions. The distributions show the non-spherical bonding electron and anisotropic anharmonic thermal vibration of atoms. The ED along the Ti–O bond is good agreement with the first principles calculations and molecular orbital calculations at ambient conditions [10,11,13,14,28].

Numbers of 3d-electrons of Ti (atomic number 22) are reduced with more ionization. Sr (atomic number 38) has an outer shell electron (valence electron) orbitals of only 5s electron which is a spherical electron orbital. The D-F map at ambient conditions in Fig. 2 shows the $d-p-\pi$ hybridization between t_{2g} electron of Ti(3d) and p_x electron of O(2p). Obvious residual ED is not observed around Ti ions at the tetragonal phase. The ED distribution around Ti with increasing pressure is presented in Fig. A.2 in Appendices. These maps prove the more localization of ED, resulting in more ionic character. The localized ED and more ionic character in the tetragonal phase are enhanced with increasing pressure above P_c in the D-F map. The ED in the cubic STO shows a gradual disappearance of the π bond character with successive pressure.

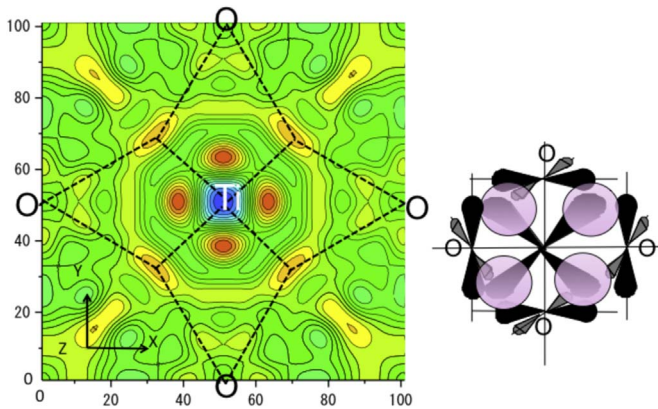


Fig. 2. Residual electron density distribution in the D-F maps on the (001) plane of the SrTiO₃ cubic phase at ambient conditions shows the $d-p-\pi$ hybridization between t_{2g} electron of Ti(3d) and p_x electron of O(2p). TiO₆ octahedron in the cubic phase has the site symmetry of $m3m$. Dotted lines show the $d-p-\pi$ hybridization.

Previously we found the same bonding nature of the $d-p-\pi$ bond in the octahedral site in the ferroelectric orthorhombic perovskite KNbO₃ [29] and ferroelectric tetragonal perovskite PbTiO₃ by maximum entropy method (MEM) using the X-ray single crystal diffraction intensities. *Ab initio* model calculation [30] proves O valence electrons in BaTiO₃ are strongly hybridized with Ti. The ED feature around Ti at ambient conditions accords with the ED calculations [22,31]. Sr valence shell electrons do not exhibit asphericity and deformation of the electron orbital, because of 5s electron. However, ED map shows the strong deformation of ED distribution around the Sr atom. The very similar positive peaks are found around the Ti atom. These characteristic features are related to an anisotropic anharmonic thermal vibration of both atoms.

The difference of Ti–O and Sr–O bond distances in the tetragonal phase can be explained by Fig. A.1, in which show the D-F maps of the tetragonal phase at 10.28 GPa and 80 K. The thermal vibration of the O1 atom interprets two positive peaks along the c axis around O1 in the map at 80 K. Electron densities of both Ti and Sr are elongated to the direction of the c axis. The $c/a > 1$ of the tetragonal phase at low-temperature can be explained by the positional disorder in the direction of the c axis. The D-F map at 10.28 GPa proves the residual electron density is elongated to the a -direction. The two maps specify the difference in thermal dynamical vibration of atoms of the tetragonal phases under low-temperature and high-pressure conditions.

5. Anharmonic thermal parameter

The distortion of ferroelectric substance is disclosed by the thermal vibration of atoms, which is introduced as temperature factors (thermal parameter) in the structure refinement. Temperature factor $T_{ij}(hkl)$ is an indicator of the atomic positional disorder (lattice average) and dynamical disorder (time average) of the atomic vibration in the crystal structure. The present study was initiated by refinement of the harmonic thermal vibration model with the second-order temperature coefficients. Harmonic oscillation of atom, however, cannot make any shift of the atomic position, because the harmonic potential do not shift the minimum of the parabolic potential well.

From an X-ray diffraction analysis, anharmonic thermal vibrations of all atoms are enhanced with thermal energy and cause the deformation of the lattice [26]. On the other hand, the localization of

the valence electron around the cation position is more enhanced under higher-pressure. The large positive peaks in the ED map at the Sr and Ti position is induced by the thermal parameter $T(hkl)$.

Anharmonic thermal analyses of titanate and niobate perovskite have been performed using synchrotron radiation and hot neutrons [32,33]. The motions of the split atom model and the rotator model together with the order-disorder *versus* displacive character are obtained in the present phase transition.

We studied the influence of anharmonicity on the diffraction intensities observed at variable low-temperatures. We adopted a multimodal distribution in the probability density function using cumulant expansion and Gram-Charlier series expansion [34,35].

We take into account in the temperature-factor of $T_{ij}(hkl)$ in Eq. (1) up to fourth-rank. Since the factors above fifth-rank have a large correlation with each other, they are not reliable. Consequently they are not applied in the calculation. The anharmonic temperature factor equation of the cumulant and Gram-Charlier series expansions are detailed in Table A.3 in Appendices. They can be interpreted by the atomic positional disorder and atomic vibration in the crystal structure. Electron density D-F maps of cubic STO based on harmonic model (left side) and anharmonic oscillation model (right side) are presented in Fig. 3.

Anharmonic model in the tetrahedral phase at low-temperatures reveals a large anisotropy in both Sr and Ti. Anharmonic thermal vibrations of O (including O1 and O2) in both cubic and tetragonal

phases are more obvious than Sr and Ti. O1 and O2 show noticeable anisotropic anharmonic parameters below T_c , as shown Fig. 3. O2 has a variable positional parameter and more flexibility than O1, because the latter is located at the crystallographically special position.

6. Molecular orbital (MO) calculation and Mulliken charge

The electronic structures, (band structure, density of state and ED distribution), have been examined with emphasis on the covalency effects of ferroelectrics. Structure studies of dynamical properties of perovskites have been published by LDA [36] and the local spin density approximation was reported by GGA calculations [37]. The electronic structure of a wide range of perovskites was examined using *ab initio* HF method [38]. A number of different approximations correlation functional including hybrid exchange techniques have been developed. Many methods are compared with previous quantum mechanical calculations [11–14].

In the present study, besides the D-F calculation, *ab initio* calculation of the electronic structure is performed using the quantum chemical MO calculation program package of Gaussian-09 [38]. Structural models are based on the atomic coordinates experimentally determined by the precise structure analyses by single crystal X-ray diffraction study. The results of the calculation are visualized by program GaussianView [39], which is the advanced and powerful graphical interface available for Gaussian-09.

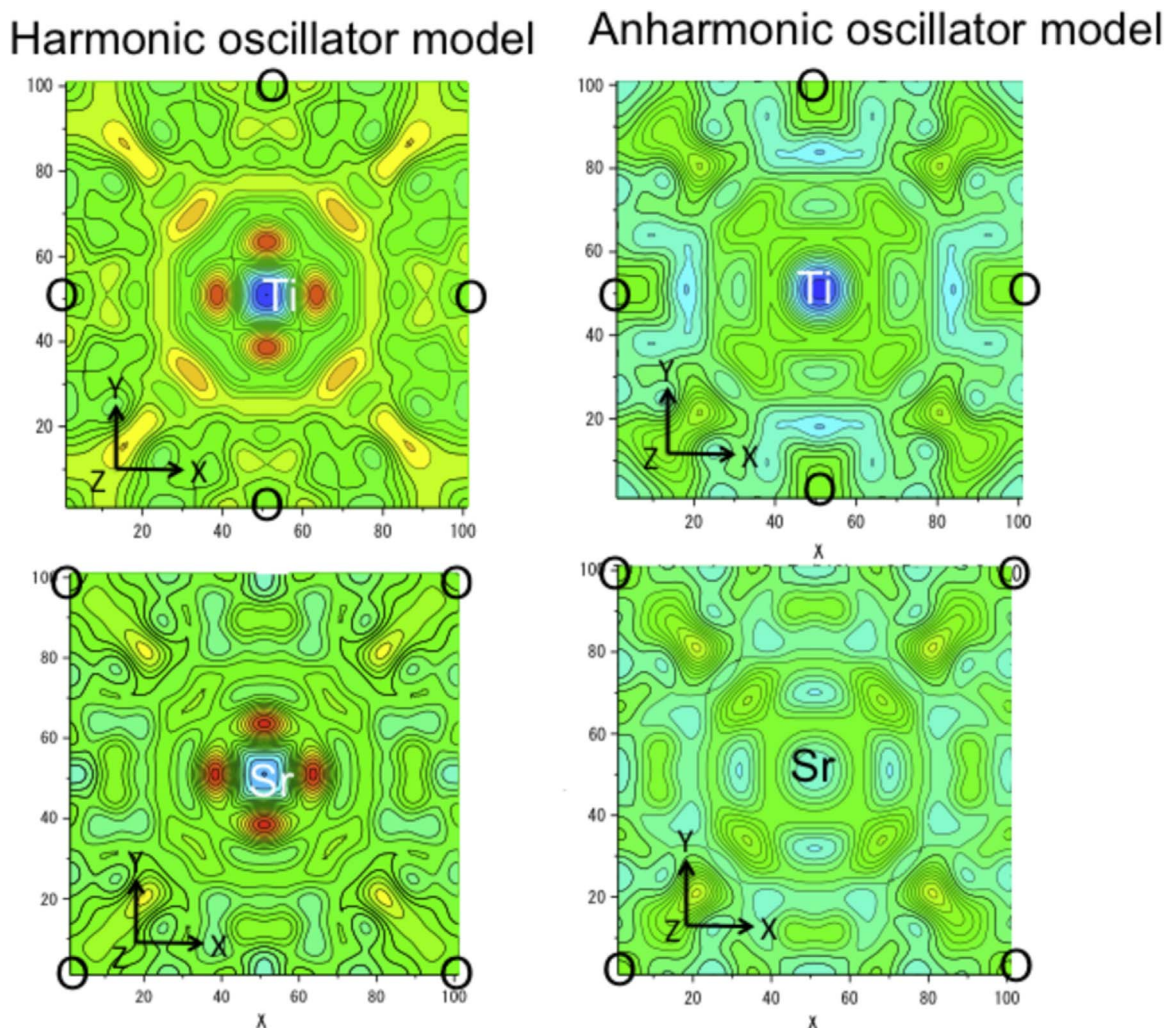


Fig. 3. Harmonic oscillation model (left side) and anharmonic model (right side) in the D-F map on (001) plane show the ED distributions at the TiO_6 and SrO_8 polyhedron at ambient conditions. Four positive peaks near Ti and Sr atoms in the cubic phase found in harmonic model disappear in consideration of anharmonic thermal vibration atoms.

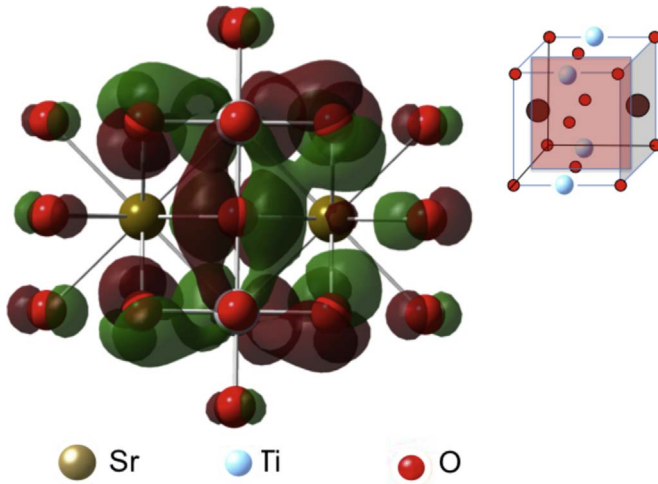


Fig. 4. MO calculation is executed using the method of HF and basis set of 3–21G. In the MO on the projection perpendicular to the (010) direction, Red and green colors are positive and negative orbitals, respectively. Hybridization between Ti(3d) and O(2p) at the TiO₆ octahedral site forms a $d-p-\pi$ bond. Obvious hybridization is not found around Sr atom.

We applied HF and DFT for all calculations using program Gaussian-09 at different pressures and temperatures with the 3–21G and 6–31G basis set. We applied several structure models including Sr, Ti and O together with H atoms to avoid the lone-paired electrons of oxygen. The selected structure models are the distribution of atoms perspective to (100), (110) and (111) directions. The sizes of molecules are limited because of the computer limitation.

Surface of the highest occupied molecular orbitals (HOMO) surface at various pressures and temperature are presented in Fig. A.4 and Fig. A.5 in Appendices. High-energy orbital surface indicates the $d-p-\pi$ bond between Ti and O, which is shown in Fig. 4. The orbitals clearly show the π bond in the figure. The calculated MO figures are in accordance with the D-F map observed by the residual ED distribution

of the $d-p-\pi$ bond. No bonding orbital is found in MO around Sr atoms, because valence electron of Sr is 5s. Since MO calculation reveals the static electron orbits, it does not disclose the atomic vibration of atoms.

Mulliken charges indicate the effective charges for Sr, Ti and O ions. The calculated charges are presented at variable temperatures and pressure in Table 2. The charges of Ti, Sr and O are much smaller than their formal ionic charges. The covalent nature of the Ti–O bond is proved, as already discussed from the residual ED in the D-F map. However, the charge of Sr remains a little closer to the formal charge. In the tetragonal structure at high-pressures above P_c , Ti and Sr increase their ionic characters (formal charge of 4e and 2e respectively). Mulliken charges of Ti, Sr and O increase their ionicity with changing structure from cubic to tetragonal at high-pressures above P_c : Ti (1.79e to 1.99e), Sr (1.17e to 1.23e) and O (–0.88e to –0.94e) and at low-temperatures below T_c : Ti (1.79e to 1.85e), Sr (1.17e to 1.18e) and O (–0.88e to –0.89e). The charge of Ti ion increases with increasing pressure and lowering temperature. It infers the perovskite structure is composed of the rigid octahedra of TiO₆. But Sr atom seems to be placed in the open space. Ti–O1 bond parallel to the z-axis becomes shorter but Ti–O2 bond is elongated by the rotation in the $x-y$ plane in the structure. The ionicity is accelerated in the tetragonal phase. Trigger of the rotation may be induced by the approach of the compression toward the limit of the Ti–O bonds of antiferroelectric tetragonal phase with $I4/mcm$.

7. Conclusion

Precise diffraction intensity measurement at extreme conditions can be undertaken using highly collimate beam with point detector of scintillation counter on high power rotated anode X-ray generator. Residual electron densities found in the D-F maps interpret the electron hybridization of $d-p-\pi$ bond of Ti(3d) and O(2p) electron around octahedral Ti atom. However, electron deformation is not found around Sr. Electron densities ascribed to the dynamical disorder can be discussed only by anisotropic anharmonic thermal vibration of atoms in consideration of higher order tensors than the conventional

Table 2

Mulliken charges of all atoms in STO are individually determined by using the model of HF/3–21G. The calculated charge of O_{calc} is defined for the neutrality of the bulk crystal. Those of O1(–2e) and O2(–2e) are different each other and they are not same as O_{calc} , because H atoms are imaginary added to O1 and O2 to neglect the lone-paired coordination.

| Bond distance and Mulliken population change at high pressure | | | | | |
|---|--------|------------|----------|---------|------------|
| | | cubic | $Pm3m$ | | |
| P (GPa) | Sr(2e) | Ti(4e) | O(–2e) | | O_{calc} |
| 0.0001 | 1.174 | 1.786 | –0.883 | | –0.987 |
| 1.35 | 1.032 | 1.874 | –0.850 | | –0.968 |
| 5.10 | 0.949 | 1.883 | –0.894 | | –0.944 |
| | Sr(2e) | tetragonal | $I4/mcm$ | | |
| 7.38 | 1.133 | Ti(4e) | O1(–2e) | O2(–2e) | O_{calc} |
| 10.28 | 1.141 | 1.929 | –0.934 | –0.906 | –1.021 |
| 11.88 | 1.227 | 1.948 | –0.936 | –0.914 | –1.030 |
| | | 1.989 | –0.935 | –0.921 | –1.072 |
| Bond distance and Mulliken population change at low temperature | | | | | |
| | | cubic | $Pm3m$ | | |
| T (K) | Sr(2e) | Ti(4e) | O(–2e) | | O_{calc} |
| 300 | 1.174 | 1.786 | –0.883 | | –0.987 |
| 190 | 0.925 | 1.830 | –0.890 | | –0.918 |
| 120 | 0.865 | 1.834 | –0.895 | | –0.899 |
| 100 | 0.864 | 1.834 | –0.896 | | –0.899 |
| | Sr(2e) | tetragonal | $I4/mcm$ | | |
| 95 | 1.131 | Ti(4e) | O1(–2e) | O2(–2e) | O_{calc} |
| 80 | 1.177 | 1.886 | –0.891 | –0.904 | –1.005 |
| | | 1.850 | –0.894 | –0.907 | –1.009 |

second-rank thermal parameters, because the parameters are based on harmonic oscillator model indicating parabolic potential of atomic vibration. The pressure dependence of the residual electron densities suggests that the electron density is more localized and more ionized with elevating pressure.

The compressions of the lattice constants of a and c of tetragonal phase are noticeably decreased at pressures above P_c . The lattice distortion of $c/a < 1$ of the tetragonal phase becomes more intensified with increasing pressure. On the other hand the ratio at low temperature below T_c is $c/a > 1$ and increases with lowering temperature. The difference in the lattice constants is induced by rotation of O2 atomic positions in two phases between high-pressure and low-temperature experiments.

Ab initio MO calculation of the electronic structure examines the ionic effects of STO under high-pressure and low-temperature conditions. Observed Mulliken charges of Ti, Sr and O are much smaller charges than their formal ionic charges. The increase in their charges indicates more ionic at the transition from cubic to tetragonal above P_c and below T_c , which is coincident with the experimental results of the D-F observations.

Acknowledgement

We greatly appreciate Dr. A. Kyono in Division of Earth Evolution Sciences, Graduate School of Life and Environmental Sciences, University of Tsukuba for the sample preparation and also express our great thanks to Dr. Y. Nakamoto and Dr. M. Sakata, Center for Science and Technology Under Extreme Conditions, Osaka University for their help for the sample pressurization. This work was supported as a part of EFREE, an Energy Frontier Research Center funded by the US Department of Energy (DE-SC-0001057; SAG) and NSF Grants EAR-1345112 and EAR-1447438. This work was also partially supported by the Natural Science Foundation of China (Grant no. U1530402).

Appendix A. Supporting information

Supplementary data associated with this article can be found in the online version at [doi:10.1016/j.ssc.2016.10.009](https://doi.org/10.1016/j.ssc.2016.10.009).

References

- [1] P.A. Fleury, J.F. Scott, J.M. Worlock, *Phys. Rev. Lett.* 21 (1968) 16.
- [2] H. Thomas, K.A. Müller, *Phys. Rev. Lett.* 21 (1968) 1256.
- [3] K.A. Müller, H. Burkard, *Phys. Rev. B* 19 (1979) 3593.
- [4] K.A. Müller, W. Berlinger, E. Tosatti, *Z. Phys. B* 84 (1991) 277.
- [5] R. Viana, P. Lunkenheimer, J. Hemberger, R. Böhmer, A. Loidl, *Phys. Rev. B* 50 (1994) 601.
- [6] F. Schooley, W.R. Hosler, M.L. Cohen, *Phys. Rev. Lett.* 12 (1964) 474.
- [7] T. Ishidate, T. Isonuma, *Ferroelectrics* 137 (1992) 45.
- [8] M. Guennou, P. Bouvier, J. Kreisel, *Phys. Rev. B* 81 (2010) 054115.
- [9] W. Zhong, D. Vanderbilt, *Phys. Rev. B* 53 (1996) 5054.
- [10] N. Sai, D. Vanderbilt, *Phys. Rev. B* 62 (2000) 13942.
- [11] H. Salehi, *J. Mod. Phys.* 2 (2011) 934.
- [12] C.E. Ekuma, D. Bagayoko, M. Jarrell, J. Moreno, *Mater. Sci. Condens. Matter* (2012). <http://dx.doi.org/10.63/1.4751260>.
- [13] S. Piskunov, E. Heifets, R.I. Eglitis, G. Borstel, *Comput. Mater. Sci.* 29 (2004) 165.
- [14] E. Heifets, R.I. Eglitis, E.A. Kotomin, J. Maier, G. Borstel, *Surf. Sci.* 513 (2002) 211.
- [15] N.V. Krainyukova, V.V. Butskii, *Surf. Sci.* 454–456 (2000) 628.
- [16] L. Rimai, G.A. deMars, *Phys. Rev.* 127 (1962) 702.
- [17] S.A. Hayward, E.K.H. Salje, *J. Phys. Chem. Solids* 61 (1999) 305.
- [18] M.A. Carpenter, *Am. Mineral.* 92 (2007) 309.
- [19] E.K.H. Salje, M. Guennou, P. Bouvier, M.A. Carpenter, J. Kreisel, *J. Phys. Condens. Matter* 23 (2011) 275901.
- [20] E.N. Maslen, N. Spadaccini, T. Ito, F. Marumo, Y. Satow, *Acta Cryst.* B51 (1995) 939.
- [21] Y.A. Abramov, V.G. Tsirelson, V.E. Zavodnik, S.A. Ivanov, I.D. Brown, *Acta Cryst.* B51 (1995) 942.
- [22] W. Jauch, M. Reehuis, *Acta Cryst.* A61 (2005) 411.
- [23] R. Ranjan, D. Pandey, N.P. Lalla, *Phys. Rev. Lett.* 84 (2000) 3726.
- [24] E.A. Zhurova, V.G. Tsirelson, *Acta Cryst.* B58 (2002) 567.
- [25] V. Tsirelson, A. Stash, *Acta Cryst.* B58 (2002) 780.
- [26] T. Yamanaka, T. Fukuda, T. Hattori, *Rev. Sci. Instrum.* 72 (2001) 1458.
- [27] H.K. Mao, J. Xu, P.M. Bell, *J. Geophys. Res.* 91 (1986) 4673.
- [28] J. Friis, B. Jiang, J. Spence, K. Marthinsen, R. Holmestad, *Acta Cryst.* A60 (2004) 402.
- [29] T. Yamanaka, T. Okada, Y. Nakamoto, *Phys. Rev. B* 80 (2009) 094108.
- [30] P. Blaha, K. Schwarz, P. Dufek, G. Vielsack, W. Weber, *Z. Nat.* 48a (1993) 129.
- [31] R.E. Cohen, H. Krakauer, *Phys. Rev. B* 42 (1990) 6416.
- [32] J. Hutton, R.J. Nelves, *J. Phys. C Solid State Phys.* 14 (1981) 1713.
- [33] J.M. Kiat, G. Baldinozzi, M. Dunlop, C. Malibent, B. Dkhil, C. Menoret, O. Masson, M.T. Fernandez-Diaz, *J. Phys. Condens. Matter* 12 (2000) 8411.
- [34] T. Yamanaka, Y. Takeuchi, M. Tokonami, *Acta Cryst.* B40 (1984) 96.
- [35] T. Yamanaka, M. Ahart, Y. Nakamoto, Z.G. Ye, S.A. Gramsch, H.K. Mao, R.J. Hemley, *Phys. Rev. B* 86 (2012) 174108.
- [36] R.D. King-Smith, D. Vanderbilt, *Phys. Rev. B* 49 (1994) 5828.
- [37] S. Tinte, M.G. Stachiotti, *Phys. Rev. B* 58 (1998) 11959.
- [38] F. Cora, C.R.A. Catlow, *Faraday Discuss.* 114 (1999) 421.
- [39] M.J. Frisch, G.W. Trucks, H.B. Schlegel, G.E. Scuseria, M.A. Robb, J.R. Cheeseman, G. Scalmani, V. Barone, B. Mennucci, G.A. Petersson, et al., *Gaussian 09, Revision A.1*, Gaussian, Inc., Wallingford, Connecticut, 2009.